LAWRENCE
LIVERMORE
NATIONAL
LABORATORY

LLNL-JRNL-665469

Phase-field modeling of diffusional phase behaviors of solid surfaces: A case study of phase-separating LiXFePO4 electrode particles

T. W. Heo, L. Q. Chen, B. C. Wood

December 16, 2014

Computational Materials Science

Disclaimer

This document was prepared as an account of work sponsored by an agency of the United States government. Neither the United States government nor Lawrence Livermore National Security, LLC, nor any of their employees makes any warranty, expressed or implied, or assumes any legal liability or responsibility for the accuracy, completeness, or usefulness of any information, apparatus, product, or process disclosed, or represents that its use would not infringe privately owned rights. Reference herein to any specific commercial product, process, or service by trade name, trademark, manufacturer, or otherwise does not necessarily constitute or imply its endorsement, recommendation, or favoring by the United States government or Lawrence Livermore National Security, LLC. The views and opinions of authors expressed herein do not necessarily state or reflect those of the United States government or Lawrence Livermore National Security, LLC, and shall not be used for advertising or product endorsement purposes.

Phase-field modeling of diffusional phase behaviors of solid surfaces : A case study of phase-separating Li_XFePO_4 electrode particles

Tae Wook Heo[1*], Long-Qing Chen[2], Brandon C. Wood[1]

[1]Materials Science Division, Lawrence Livermore National Laboratory, Livermore, California 94550, USA
[2]Department of Materials Science and Engineering, The Pennsylvania State University, University Park, Pennsylvania 16802, USA

Abstract

We present a comprehensive phase-field model for simulating diffusion-mediated kinetic phase behaviors near the surface of a solid particle. The model incorporates elastic inhomogeneity and anisotropy, diffusion mobility anisotropy, interfacial energy anisotropy, and Cahn-Hilliard diffusion kinetics. The free energy density function is formulated based on the regular solution model taking into account the possible solute-surface interaction near the surface. The coherency strain energy is computed using the Fourier-spectral iterative-perturbation method due to the strong elastic inhomogeneity with a zero surface traction boundary condition. Employing a phase-separating Li_XFePO_4 electrode particle for Li-ion batteries as a model system, we perform parametric three-dimensional computer simulations. The model permits the observation of surface phase behaviors that are different from the bulk counterpart. For instance, it reproduces the theoretically well-established surface modes of spinodal decomposition of an unstable solid solution: the *surface mode of coherent spinodal decomposition* and the *surface-directed spinodal decomposition mode*. We systematically investigate the influences of major factors on the kinetic surface phase behaviors during the diffusional process. Our simulation study provides insights for tailoring the internal phase microstructure of a particle by controlling the surface phase morphology.

Keywords: Phase-field model; Solid surface; Phase behavior; Electrode particle

**E-mail address*: heo1@llnl.gov

Release number: LLNL-JRNL-665469

Highlights

- A phase-field model for diffusional phase behaviors of a solid surface is presented.
- A phase-separating Li_XFePO_4 electrode particle is employed as a model system.
- The model reproduces the well-established surface spinodal decomposition modes.
- The effects of major physical factors on the surface phase behaviors are examined.
- The surface phase configuration can control the internal phase microstructure.

1. Introduction

The successful development of electrode materials for Li-ion batteries is intimately connected to the understanding of their phase transitions during electrochemical cycles. The thermodynamics and kinetics of the phase behaviors significantly affect the charge storage capacity and the rate performance of batteries. A number of associated scientific challenges at the electrode level have been proposed, leading to extensive computational and experimental investigations over a decade for better understanding the relevant phase transformation mechanisms [1]. To elucidate the governing physical mechanisms of the phase behaviors, Li_XFePO_4 has been intensively studied as a model electrode system since it is considered as a promising cathode material for large-scale applications [2]. For example, Delacourt *et al.* observed various possible metastable solid solution phases upon cooling although Li_XFePO_4 is a strong phase-separating material [3]. Yamada *et al.* demonstrated a miscibility gap in Li_XFePO_4 at room temperature [4]. Meethong *et al.* experimentally showed the particle size effects on the miscibility gap in nanoscale Li_XFePO_4 [5]. They also discussed the roles of strain accommodation during lithiation/delithiation cycles in the phase transformation behavior [6]. Gibot *et al.* suggested that the particle size and stoichiometry of Li_XFePO_4 determine whether it undergoes single- or two-phase lithiation/delithiation processes using numerous experimental and analytical methods [7]. Van der Ven *et al.* provided a theoretical explanation on the effects of coherency strain on the phase stability of intermediate solid solutions of Li_XFePO_4 at low temperatures [8], and Wagemaker, Mulder, and Van der Ven theoretically discussed the role of surface and interfacial energy in the phase stability of nanosized Li_XFePO_4 particles [9]. Malik, Zhou, and Ceder showed the possible single-phase transformation pathway of Li_XFePO_4 at very low overpotential employing canonical Monte Carlo simulations [10]. Ichitsubo *et al.* explored the effects of elastic energy and interfacial energy on the phase separation behavior of Li_XFePO_4 in terms of thermodynamics and kinetics emphasizing the concept of a preferred wavelength of spinodal decomposition [11].

The phase-field approach [12-16] has been regarded as one of the most suitable computational methods for modeling the phase microstructures of electrode materials. The first development of the phase-field model for the electrochemical intercalation process in a simple two-phase system was done by Han and collaborators [17]. As an extension of Han *et al.*'s model [17], Singh, Ceder, and Bazant developed the so-called Cahn-Hilliard reaction (CHR) model based on the gradient thermodynamics employing the depth-averaged concentration concept that is valid for the surface-reaction-limited kinetics [18]. The model incorporates the Li insertion/extraction reaction at the electrode/electrolyte interface for phase-separating systems such as Li_XFePO_4, and proposes a scheme based on phase transformation wave (or intercalation wave) kinetics. Burch and Bazant investigated the effects of Li_XFePO_4 particle size on the miscibility gap and demonstrated the shrinking characteristics upon decreasing particle size employing the CHR model [19]. Bai, Cogswell, and Bazant investigated the effect of the current density on the phase transformation [20], and Cogswell and Bazant discussed the effect of the coherency strain on the kinetics of the phase separation [21] and the nucleation behavior [22] in Li_XFePO_4 nanoparticles also employing the CHR model. A detailed review of the CHR model is also available [23]. Apart from the CHR model, other types of phase-field models have been also developed and applied to Li_XFePO_4. Tang *et al.* proposed the phase-field model to study the crystalline to amorphous phase transformation in nanoscale olivines and assessed the effects of particle size, applied electrical overpotentials, and misfit strain on the phase stabilities and phase transformation pathways [1, 24, 25]. In addition, Tang, Belak, and Dorr explained the physical origin of the anisotropic growth morphology of the phase boundary between Li-rich and Li-lean phases employing the phase-field model [26]. They found that the misfit strain and the one-dimensional Li diffusivity play a key role in determining the growth morphology. Recently, Ichitsubo *et al.* studied the effects of coherent strain energy on the behaviors of phase separation taking place through nucleation-and-growth as well as spinodal mechanisms and discussed the stabilities of phase boundaries employing the phase-field method [27].

Surfaces often also play a significant role in determining the surface phase segregation and/or phase transformation behaviors, since a battery electrode usually consists of a number of solid-state particles. A solid surface is a two-dimensional structural defect where many abrupt changes of physical properties may occur; hence, its presence is likely to modify the thermodynamics and kinetics of phase transformations. Therefore, the understanding of surface effects on phase microstructures is an additional critical factor for controlling the internal phase behaviors and achieving better battery performance. In light of this, we present our comprehensive phase-field model for simulating phase microstructure evolution in the presence of surfaces. Employing Li_XFePO_4 as a model system, we show how our model is able to reproduce known surface phase transition mechanisms, and can be used to systematically assess the effects of various physical factors on the surface phase evolution.

2. Phase-field model

To describe the diffusional phase behavior in a binary system, we employ the solute composition $X(\vec{r})$ as a field variable. The free energy functional of an entire solid-state system in the context of the diffuse-interface description [28] is given by:

$$F = \int_V [f_{inc}(X,T) + f_{grad}(\vec{\nabla}X) + f_{coh}(\varepsilon_{ij},X)]d^3r, \tag{1}$$

where f_{inc} is the incoherent free energy density of a local solid solution, f_{grad} is the gradient energy density ($=(\kappa_{ij}^c/2)\cdot\nabla_i X\cdot\nabla_j X$ with the anisotropic gradient energy coefficient κ_{ij}^c), and f_{coh} is the coherency strain energy density arising from the compositional inhomogeneity.

We employ a free energy density function based on the regular solution model. Solute atoms and phases interact with surfaces to relax the chemical and/or elastic strain energy in a solid particle. To model the interaction between $X(\vec{r})$ and surfaces, the surface structure is described by the domain parameter ψ in the present model as shown in Fig. 1(a). The interior of a particle is represented by $\psi = 1$, the outside of a particle is represented by $\psi = 0$, and the surface is represented by $0 < \psi < 1$. In order to describe the solute-surface interactions, we introduce an additional explicit contribution to the free energy function, resulting in the variation of the local thermodynamics near surfaces. It should be mentioned that in our model, the solute-solute interaction is not altered by the presence of surfaces (*i.e.*, the regular solution parameter does not change near surfaces). Therefore, the incoherent free energy density is given by

$$f_{inc}(X,T) = [\Omega\cdot X\cdot(1-X) + R\cdot T\cdot[X\cdot\ln X + (1-X)\cdot\ln(1-X)] - m\cdot g(\psi)\cdot X]/V_m, \tag{2}$$

where Ω is the regular solution parameter, R is the gas constant, T is the temperature, and V_m is the molar volume of a solid. The last term $[-m\cdot g(\psi)\cdot X]$ represents the solute-surface interactions [29-31], where m is the interaction parameter that determines the strength of the interaction and $g(\psi)$ $(=\psi^2(\psi-1)^2)$ is the phenomenological function of a domain parameter associated with the topology of the interaction potential that is non-zero only at the surface. Solute segregation at the surface takes place for $m>0$, whereas solute depletion is induced when *m*<0. We note that this simplified description could be refined by considering available analytical models that can incorporate specific possible physical contributions to the surface segregation energetics. Such factors include the surface energy change upon solute composition variation, atomic mismatch relaxation, excess entropy contribution, and so on [32]. In addition, anisotropic characteristics could be added to the formulation of *m*, reflecting, for example, the anisotropic surface energetic characteristics of the Li_XFePO_4 system [33]. For simplicity, we have chosen to neglect such effects here.

The coherency strain energy f_{coh} in Eq. (1) is perturbed by the presence of a free surface due to zero traction force at the surfaces (See Fig. 1(a)). To obtain the elastic solutions with the zero surface traction boundary condition ($T_i = -\sigma_{ij} \cdot n_j = 0$, where $\vec{n} = (n_1, n_2, n_3)$ is the unit surface normal), we apply the smoothed boundary method [34] to the mechanical equilibrium equation using the domain parameter ψ (*i.e.*, we solve $\psi \cdot (\partial \sigma_{ij} / x_j) = 0$). According to Khachaturyan's microelasticity theory, the stress tensor can be represented by $\sigma_{ij} = C_{ijkl}(\bar{\varepsilon}_{kl} + \delta\varepsilon_{kl} - \varepsilon^0_{kl})$, where C_{ijkl} is the elastic modulus tensor, $\bar{\varepsilon}_{kl}$ is the homogeneous strain tensor, $\delta\varepsilon_{kl}$ is the heterogeneous strain tensor, and ε^0_{kl} is the eigenstrain tensor. Substituting $\delta\varepsilon_{kl} = (1/2) \cdot (\partial u_i / \partial x_j + \partial u_j / \partial x_i)$, where $\vec{u}$ is the elastic displacement, into the mechanical equilibrium equation with the smoothed boundary method yields [34]

$$\frac{\partial}{\partial x_j}\left[\psi \cdot C_{ijkl} \cdot \bar{\varepsilon}_{kl}\right] + \frac{\partial}{\partial x_j}\left[\psi \cdot C_{ijkl} \cdot \frac{\partial u_k}{\partial x_l}\right] - \left(\frac{\partial \psi}{\partial x_j}\right) \cdot \sigma_{ij} = \frac{\partial}{\partial x_j}\left[\psi \cdot C_{ijkl} \cdot \varepsilon^0_{kl}\right] \qquad (3)$$

The original mechanical equation is reproduced when $\partial \psi / \partial x_j$ vanishes and ψ becomes 1 (*i.e.*, in the particle interior). We note that the unit surface normal can be expressed by the gradient of the domain parameter as $\vec{n} = \vec{\nabla}\psi / \left|\vec{\nabla}\psi\right|$. The zero surface traction boundary condition can be expressed by $T_i = -\sigma_{ij} \cdot (\partial \psi / \partial x_j) / \left|\vec{\nabla}\psi\right| = 0$. Therefore, the third term in Eq. (3) becomes zero by the zero surface traction boundary condition. The elastic modulus of a compositionally non-uniform solid solution is inherently inhomogeneous, and is assumed to linearly vary with the solute composition X as $C_{ijkl}(X) = C^A_{ijkl} \cdot (1 - X) + C^B_{ijkl} \cdot X$, where C^A_{ijkl} and C^B_{ijkl} are the elastic moduli of two end phases of a solid solution (*e.g.*, C^A_{ijkl} and C^B_{ijkl} can be elastic moduli of $FePO_4$

and LiFePO$_4$, respectively, with Li composition X in the case of a Li$_X$FePO$_4$ solid solution). The homogeneous strain tensor in Eq. (3) when the surfaces are allowed to relax and the elastic modulus is inhomogeneous is computed by $\bar{\varepsilon}_{kl} =< C_{ijkl}(X) >^{-1} [< \sigma^0_{ij} > - < \delta\sigma_{ij} >]$ [35-37], where $< C_{ijkl}(X) >= (1/V)\int_V C_{ijkl}(X)dV$, $< \sigma^0_{ij} >= (1/V)\int_V C_{ijkl}(X)\varepsilon^0_{kl}dV$, $< \delta\sigma_{ij} >= (1/V)\int_V C_{ijkl}(X)\delta\varepsilon_{kl}dV$, and V is the volume of a particle. The eigenstrain tensor due to the compositional inhomogeneity in Eq. (3) is modeled as $\varepsilon^0_{kl} = \varepsilon^m_{kl} \cdot X$, where ε^m_{kl} is the misfit strain between two end phases. Employing $\bar{\varepsilon}_{kl}$ and ε^0_{kl}, we solve Eq. (3) using the Fourier spectral iterative-perturbation method [38, 39].

The temporal and spatial evolution of the composition X is governed by the Cahn-Hilliard nonlinear diffusion equation [40] as follows:

$$\frac{\partial X}{\partial t} = \nabla_i \cdot \left[M_{ij} \nabla_j \left(\frac{\delta F}{\delta X} \right) \right] = \nabla_i \cdot \left[M_{ij} \nabla_j \left(\frac{\partial f_{inc}}{\partial X} - \kappa^c_{kl} \nabla_k \cdot \nabla_l X + \frac{\partial f_{coh}}{\partial X} \right) \right], \qquad (4)$$

where M_{ij} is the anisotropic interdiffusion mobility and $(\delta F / \delta X)$ is the variational derivative of F (Eq. (1)) with respect to X. Eq. (4) is numerically solved using the semi-implicit Fourier-spectral method [41, 42].

3. Computer simulations and discussions

We employ the physical parameters of orthorhombic Li$_X$FePO$_4$ (space group *Pnma*) from the literature. For the incoherent thermodynamic free energy density function (Eq. (2)), the regular solution parameter (Ω) is set to be $12 kJ/mol$ [24, 26], the molar volume (V_m) of Li$_X$FePO$_4$ is set to be $43.8 \times 10^{-6} m^3/mol$ [24, 26], and the temperature (T) is set to be $298K$. The isotropic gradient energy coefficient ($\kappa^c_{11} = \kappa^c_{22} = \kappa^c_{33}, \kappa^c_{ij}(i \neq j) = 0$) is chosen to be $5 \times 10^{-10} J/m$, resulting in $\sim 119 mJ/m^2$ of the interfacial energy. For the calculation of the coherency strain energy, the elastic constants for FePO$_4$ (*FP*) are chosen to be $C^{FP}_{11} = 175.9$, $C^{FP}_{22} = 153.6$, $C^{FP}_{33} = 135.0$, $C^{FP}_{12} = 29.6, C^{FP}_{13} = 54.0, C^{FP}_{23} = 19.6$, $C^{FP}_{44} = 38.8, C^{FP}_{55} = 47.5$, $C^{FP}_{66} = 55.6$, and those for LiFePO$_4$ (*LFP*) are chosen to be $C^{LFP}_{11} = 138.9$, $C^{LFP}_{22} = 198.0$, $C^{LFP}_{33} = 173.0$, $C^{LFP}_{12} = 72.8, C^{LFP}_{13} = 52.5$, $C^{LFP}_{23} = 45.8$, $C^{LFP}_{44} = 36.8$, $C^{FP}_{55} = 50.6$, $C^{FP}_{66} = 47.6$ (in GPa) in Voigt notation [43]. The components of the misfit strain tensor (ε_{ij}^{m}) between *FP* and *LFP* phases are computed assuming perfect interfacial coherency and using the lattice parameters of the two phases ($FePO_4$ and $LiFePO_4$): $a_{FP} = 0.98267nm$, $b_{FP} = 0.57944nm$, $c_{FP} = 0.47832nm$ and $a_{LFP} = 1.03289nm$, $b_{LFP} = 0.60069nm$, $c_{LFP} = 0.46905nm$ [6], resulting in $\varepsilon_{11}^{m} = (a_{LFP} - a_{FP})/a_{FP} = 0.05111$, $\varepsilon_{22}^{m} = (b_{LFP} - b_{FP})/b_{FP} = 0.03667$, $\varepsilon_{33}^{m} = (c_{LFP} - c_{FP})/c_{FP} = -0.01976$, and $\varepsilon_{ij}^{m} = 0.0\,(\text{when}\, i \neq j)$. The mechanical equilibrium (Eq. (3)) and the Cahn-Hilliard (Eq. (4)) equations are solved in dimensionless forms (by f_{inc}/E, $\kappa_{ij}^{c}/(E \cdot l^2)$, $\Delta x/l$,$\Delta t \cdot (M_{22}/l^2) \cdot E$, and C_{ijkl}/E, where E (= $10^9 J/m^3$) is the characteristic energy and l (=1*n*m) is the characteristic length). For simulating surface phase behaviors, we first generate the diffuse-interface surface structure represented by the domain parameter ψ in a three-dimensional ($168\Delta x \times 168\Delta x \times 168\Delta x$) computational grid with Δ*x*=1*n*m under the periodic boundary conditions. To mimic the plate-like shape particle geometry that is commonly observed in experiments [44], we employ a single particle with flat surfaces and the particle thickness *d* in the computational grid as illustrated in Fig. 1(b). We then carry out parametric simulations and monitor the phase separation behavior of an unstable solid solution of $Li_{0.5}FePO_4$ (*i.e.*, overall Li composition (X_0) =0.5 and $\partial^2 f/\partial X^2\big|_{X=X_0} < 0$, where $f = f_{inc} + f_{coh}$) into Li-rich and Li-lean phases.

3.1. Effect of solute-surface interactions

We first examined the effects of solute-surface interactions at the initial stage of phase separation of an unstable solid solution in a particle with *d*=158Δ*x*. To study the effect of the interactions on the microstructural features and their evolution kinetics, we simulated six different microstructures with the increasing interaction parameter *m* in Eq. (2). Fig. 2(a) shows the simulated microstructures at the early stages (*t*=50000Δ*t*) for different magnitudes of *m*, and Fig. 2(b) shows the volume fraction of Li-rich phases (with *X*>0.8) as a function of time. The white/gray/black colors of a simulated microstructure within a particle represent Li-rich/unseparated/Li-lean phases. In all cases, phase separation is initiated at surfaces. The separated surface phase microstructures display different features, and the separation kinetics becomes faster as *m* increases, as shown in Figs. 2(a) and (b). This may be explained in terms of the operating surface phase separation mechanisms. When m=0.0, there is no explicit interaction between solute atoms and surfaces. Instead, the surface phase separation occurs by the so-called *surface mode of coherent spinodal decomposition* (SCSD) proposed by Tang and Karma [45] due to the relaxation of coherency strain energy at surfaces. It is mediated by the zero surface traction boundary condition. Therefore, the separated microstructure displays a surface spinodal domain structure with compositional wave vectors parallel to surfaces as indicated on the *a*-*b* cross-section view (*i.e.*, lateral compositional modulation along surfaces as shown in Fig. 2(c)).

On the other hand, a different phase separation mode seems to operate as the strength of the solute-surface interaction (m) increases in Fig. 2(a). To further isolate the mode operated by only the solute-surface interaction term, we carried out a controlled simulation without coherency strain energy contributions for non-dimensionalized m^*=0.25. As shown in Fig. 2(d), the interaction induces surface segregation of Li that acts as the dominant perturbation of the surface composition over natural thermal fluctuations, resulting in surface-initiated spinodal decomposition. Its surface phase microstructure displays the alternating layer structure with a compositional wave vectors normal to the surface. This is the so-called *surface-directed spinodal decomposition mode* (SDSD) [46-50], which arises due to the preferential attraction of a particular component (Li in this case) to surfaces. Therefore, as m increases in Fig. 2(a), another spinodal decomposition mode (*i.e.*, SDSD) starts operating in addition to the existing coherency strain relaxation-induced spinodal mode (*i.e.*, SCSD). As a result, the surface phase microstructure for m^*=0.25 (see Fig. 2(e)) displays two different types of compositional waves. The results in Fig. 2 confirm that our model reproduces the possible well-established surface spinodal decomposition modes that arise from mechanistically different processes. Note that similar simulated phase behaviors in a thin film have been also reported [51]. We also checked that the bulk coherent spinodal decomposition mode operates in the particle interior at later stages of evolution in all of our tested cases, as proposed in Ref. [45].

It is expected that the abovementioned surface modes become increasingly dominant over the bulk modes as the particle size decreases. To investigate the relative contributions of the surface modes with decreasing particle size, additional systematic simulations were performed for several different particle size dimensions (d) based on the setup in Fig. 1(b). For better computational efficiency, we chose the computational grid size depending on the particle dimension as $(d+10)\Delta x\times(d+10)\Delta x\times(d+10)\Delta x$ (The $10\Delta x$ grid space was assigned to the outside of a particle). The diffusion mobility (M_{ij}) in Eq. (4) was assumed to be isotropic, and two different interaction parameters (m^*=0.00 and m^*=0.25) were employed. The overall composition (X_0) was also chosen to be 0.5. Figs. 3(a) and (b) shows the *a*-*b* cross-section view of simulated phase microstructures with different size dimensions (*d*) at t=100000Δt for m^*=0.0 and m^*=0.25, respectively. As clearly shown in the figures, the operating surface phase separation mode becomes increasingly significant to the phase microstructure of the entire particle as *d* decreases. For example, when the particle dimension is extremely small (*d*=14*n*m), the internal microstructure of the particle with *m*=0.0 is predominantly determined by SCSD, whereas that with m^*=0.25 is predominantly determined by SDSD. As a result, the phase microstructures within the particle interiors are very different depending on the magnitudes of m^* (*i.e.*, strength of the surface-solute interaction). Significantly, our simulation results indicate the existence of a critical particle size dimension (here, between 14*n*m and 26*n*m) below which the internal phase microstructure should be entirely controlled by the surface modes.

3.2. Effect of anisotropic and inhomogeneous diffusion mobility

The physical properties of a solid particle can be anisotropic due to its intrinsic crystallographic structure [52]. For example, the diffusion mobility of Li in a Li_XFePO_4 particle is anisotropic since its crystal structure is orthorhombic: in particular, diffusion along the *b* crystallographic axis can be much faster than other directions [53, 54]. To examine the role of anisotropic diffusion mobility in the presence of a surface, we conducted simulations employing a particle (d=158Δx) with $M_{11}(=M_{33})/M_{22}$=0.001. We chose *m*=0.0 in order to focus on the effects of the diffusion mobility anisotropy without complication from explicit surface-solute interactions. Fig. 4(a) shows the snapshots of temporal evolution during the phase decomposition at the early stage. First of all, the phase separation first occurs at surfaces as expected. Since we chose *m*=0.0, one might expect that only SCSD should operate according to the discussion in the previous section. However, in this case, the development of compositional fluctuations with wave vectors aligned along *a* and *c* directions may be extremely sluggish due to the low diffusion mobility along these directions. As a result, in contrast to Fig. 2, which is based on a case where diffusion mobility is isotropic (see Figs. 2(a) (*m*=0.0 case) or 2(c)) and the surface compositional waves with wave vectors along *a* and *c* directions are dominant, the surface mode with the compositional wave vector aligned along the *b* direction seems to occur as shown in Fig. 4(a) (see the microstructure at t=200000Δt and the *a*-*b* cross section view of the microstructure). It should be noted that this mode is qualitatively different from SDSD since no explicit solute-surface interactions are included.

The results of Fig. 4(a) can be theoretically rationalized by examining the dispersion relation $\omega(\vec{k})$ for the given surface compositional wave of $X \sim e^{i\vec{k}\cdot\vec{r}}e^{\omega t}$ where $\vec{k} = (k_1, k_2, k_3)$ is the wave vector (k_1, k_2, and k_3 correspond to *a*, *b*, and *c* directions, respectively) and ω is the kinetic amplification factor. Linearizing Eq. (4) about X=X_0 yields the following dispersion relation for the anisotropic system where the only diagonal components of M_{ij} and κ^c_{ij} in Eq. (4) are nonzero:

$$\begin{aligned}\omega(\vec{k}) &= -[M_{11}k_1^2 + M_{22}k_2^2 + M_{33}k_3^2]\cdot[f''(X_0) + \kappa^c_{11}k_1^2 + \kappa^c_{22}k_2^2 + \kappa^c_{33}k_3^2] \\ &= -[M_{11}k_1^2 + M_{22}k_2^2 + M_{33}k_3^2]\cdot[f''_{inc}(X_0) + \kappa^c_{11}k_1^2 + \kappa^c_{22}k_2^2 + \kappa^c_{33}k_3^2 + B(\vec{n})],\end{aligned} \tag{5}$$

where f'' and f''_{inc} are the second derivatives of $[f_{inc} + f_{coh}]$ and f_{inc}, respectively, with respect to X. $B(\vec{n})$ in Eq. (5) is the coherency strain energy density in the reciprocal space [55], and is given by $B(\vec{n}) = C_{ijkl}\varepsilon^m_{ij}\varepsilon^m_{kl} - n_i\sigma^0_{ij}\Omega_{jl}(\vec{n})\sigma^0_{lm}n_m$. Here, $\vec{n} = \vec{k}/|\vec{k}|$, ε^m_{ij} is the misfit strain tensor between the two end phases (*e.g.*, $FePO_4$and $LiFePO_4$ in this case), $\sigma^0_{ij} = C_{ijkl}\varepsilon^m_{kl}$, $\Omega^{-1}_{ij}(\vec{n}) = C_{iklj}n_k n_l$, and the homogeneous C_{ijkl} is denoted $C_{ijkl}(X_0)$. We note that $B(\vec{n}) \neq 0$ inside the bulk and $B(\vec{n}) = 0$ at the surface layers. A detailed derivation of Eq. (5), along with computed maximally growing wavelengths for the cases simulated in this article, is given in the Appendix.

Since f''<0 for an unstable coherent solid solution, the form of Eq. (5) implies that we may expect that the spinodal decomposition mode with its wave vector aligned along with a particular direction *i* (among *a*, *b*, and *c* orthogonal directions) is likely to be dominant as M_{ii} becomes larger and/or κ^c_{ii} becomes smaller. At a surface layer (aligned along the *a*-*c* plane in our simulation setup) where the coherency strain energy vanishes due to the zero surface traction boundary condition, the decomposition modes with wave vectors along the *a* and *c* directions are predominant with respect to the *b* direction counterpart. The coherency strain energy below the surface layer acts as a barrier for the development of the compositional wave along the *b* direction, while the development of the surface compositional waves along the *a* and *c* directions is free from any such barrier, resulting in the rapid formation of compositional waves with k_1- and k_3-wave vectors [45] if diffusion is sufficiently facile. However, if the diffusion mobility along the *a* and *c* directions is extremely low compared to that along the *b* direction, the occurrence of the compositional waves with k_1- and k_3-wave vectors may be suppressed. In this instance, compositional fluctuations with the k_2-wave vector can also occur instead. Note that this relies on the assumption that the prohibition of the k_1- and k_3-wave development by the low diffusion mobility along the *a* and *c* directions is relatively more effective than the suppression of the k_2-wave occurrence by the coherency strain energy. In fact, the non-dimensionalized amplification factor against the surface-localized compositional fluctuations with $\vec{k} = (k_1, 0, k_3)$ parallel to surfaces ($\omega^{surf,*}(k_1, 0, k_3)$=5.17×10^{-5}) is three orders of magnitude smaller than that against the fluctuation along $\vec{k} = (0, k_2, 0)$ ($\omega^{surf,*}(0, k_2, 0)$= 5.17×10^{-2}) based on Eq. (A8) (or Eq. (5) with $B(\vec{n}) = 0$). In other words, compositional fluctuations with the k_2-wave vector do in fact grow much faster than others. However, their further propagation along the *b* direction into the bulk is suppressed by the coherency strain energy. To support this analysis, we carried out a comparative simulation with less anisotropic diffusion mobility M_{11}(=M_{33})/M_{22}=0.1 (see Fig. 4(b)). It is clearly shown that the surface modes with wave vectors parallel to surfaces operate, and the compositional fluctuations with the k_2-wave vector essentially almost vanish as the diffusion mobility along the *a* and *c* axes increases.

The later stage of the phase separation behavior with highly anisotropic diffusion mobility (M_{11}(=M_{33})/M_{22}=0.001) was also monitored as shown in Fig. 4(c). As the evolution proceeds, a thin surface layer of the Li-rich phase is formed by the mode with the k_2-wave vector. Underneath this layer, this mode with the k_2-vector seems to vanish due to the associated coherency strain energy and other modes by SCSD (especially, fluctuations with the k_1-wave vector) operate, resulting in the spinodal phase domain structure. Intriguingly, the alignment of phase domains near the surface induces a *chessboard-like* microstructure within the particle interior. This is entirely due to the unique combination of anisotropic diffusion mobility and the presence of the surface. First, the domain structure *near* the surface is formed by SCSD. Next, the compositional waves propagate only along the *b* direction (normal to the surface) toward the particle interior since the uphill diffusional process occurs only along this direction. Therefore, Li-rich and Li-lean phases alternate along the *b* direction, resulting in the continuous duplication of the surface phase domain structure in a reverse fashion as the phase separation along the *b* direction proceeds. Notably, this behavior illustrates that the internal phase microstructure of a particle can be tailored by controlling the surface phase morphology. As an example of controlling the phase microstructure, let us assume that the diffusion mobility near the surface (M_{ij}^{surf}) is isotropic due to its relative disordered structure, while that of a particle interior (M_{ij}^{bulk}) is highly anisotropic (M_{11}(=M_{33})/M_{22}=0.001) (*i.e.*, the diffusion mobility $M_{ij}(\vec{r})$ of a particle is spatially inhomogeneous). From the analysis in section 3.1, the surface phase domain structure can be regulated by the diffusion mobility near the surface; we know that if the surface diffusion mobility is isotropic, more regular surface phase domains would first form, aligned along the surface as shown in Fig. 2(c) (due to SCSD). Next, the highly anisotropic diffusion mobility of the particle interior would result in continuous duplication along the *b* direction. Note that diffusion along the *a* and *c* directions in the particle interior is less likely to occur due to the low diffusion mobility along these directions. Fig. 5(a) shows the controlled microstructure at the early stage produced by the simulation, demonstrating the formation of *chessboard-like* microstructure with the *finer* compositional modulation at surfaces. In addition, we note that the phase domain spacing may be controlled by the overall composition (X_0) as well as the interfacial energy according to the fact that the most dominant compositional wavelength (or maximally growing wavelength) ($\lambda_{\max}$) at the early stage is determined by $2\pi\sqrt{-2\kappa / f''(X_0)}$ [56]. This example further indicates that the internal phase microstructure can be tuned by controlling the surface phase morphology. In addition, the evolution of the volume fraction of Li-rich phases (see Fig. 5(b)) for the above different types of diffusion mobility shows that the phase separation kinetics at the early stage is also largely controlled by the characteristics of the diffusion mobility near the surface.

3.3. Effect of interfacial energy anisotropy

The orthorhombic crystal structure of Li_XFePO_4 may also result in anisotropy of the interfacial energy. Recently, it has been reported that {010} interface between Li-rich and Li-lean phases has significantly lower *chemical* interfacial energy than other interfaces (*e.g.*, {100} and {001} interfaces) [57]. To investigate the effects of interfacial energy anisotropy on the surface phase behaviors while the surface modes are operating, we performed a sensitivity study by varying the interfacial energy. We varied only the κ_{22}^{c} component of the gradient energy coefficient tensor to control the interfacial energy of phase boundaries aligned along {010} planes fixing interfacial energies of other orientations (*i.e.*, we fixed non-dimensionalized $\kappa_{11}^{c,*}$= $\kappa_{33}^{c,*}$=0.5). The diffusion mobility M_{ij} was deliberately chosen to be isotropic. Fig. 6(a) shows the simulated microstructures with varying {010} interfacial energy at the early stage (at t=50000Δt). As the interfacial energy decreases, thin layers parallel to {010} planes form at surfaces (as indicated in the cases with $\kappa_{22}^{c,*}$=0.2). The origin of this surface effect can be traced to the discussion of Eq. (5), which suggests that compositional fluctuations with the k_2-wave vector can become dominant if κ_{22}^{c} is small at the surface where the coherency strain energy is completely relaxed. More quantitatively, the computed amplification factors against the surface compositional fluctuations along $\vec{k}=(0,k_2,0)$ ($\omega^{surf,*}(0,k_2,0)$) are 6.46×10^{-2}, 8.60×10^{-2}, and 12.93×10^{-2} (in a dimensionless form) for $\kappa_{22}^{c,*}$=0.4, 0.3, and 0.2, respectively. Comparing these with the $\vec{k}=(k_1,0,k_3)$ counterpart ($\omega^{surf,*}(k_1,0,k_3)$=$5.17\times10^{-2}$), we conclude that the growth of compositional fluctuations with the k_2-wave vector should be dominant when $\kappa_{22}^{c,*}$=0.2. As further confirmation of the impact of the interfacial energy anisotropy, we carried out a controlled simulation without any coherency strain energy contribution for $\kappa_{22}^{c,*}=0.2$. As expected, the phase boundaries aligned along {010} planes form over the entire particle as a result of the development of the compositional waves with the k_2-wave vector as shown in Fig. 6(b). Note that this mode in the case with $\kappa_{22}^{c,*}$=0.2 in Fig. 6(a) is suppressed below the surface due to the presence of coherency strain energy that acts as a barrier for the propagation of the compositional wave with the k_2-wave vector.

Given the significant effects that anisotropies in diffusion mobility and interfacial energy can have on the surface phase microstructure (Figs. 4-6), we carried out an additional computer simulation that simultaneously include both effects. We used a diffusion mobility anisotropy of M_{11}(=M_{33})/M_{22}=0.001 and an interfacial energy anisotropy of $\kappa_{22}^{c,*}$(=0.2)<$\kappa_{11}^{c,*}=\kappa_{33}^{c,*}$ (=0.5). Fig. 7

shows the *a*-*b* cross-section view of the snap shots during the phase evolution. Note that the domain-like structure along the surface layer is caused by not the regular spinodal decomposition modes but rather by random fluctuations introduced in the beginning of the simulation. It results in less uniform spacing between domains compared to other domain structures created by operating decomposition modes (for example, see Fig. 2(c) for comparison). The surface phase domain features seem to propagate through the particle interior as the separation evolves. Interestingly, the surface phase domains coarsen at the later stage (see the indicated surface phase microstructures at t=200000Δt and 300000Δt in Fig. 7) due to the relatively high interfacial energies along {100} and {001} planes compared to the interfacial energy along {010} planes, whereas the early stage phase domain features continue propagating through the bulk as the evolution proceeds. We should emphasize here that when the diffusion mobility is highly anisotropic, the surface phase domain structure at the early stage controls the internal phase microstructure at the later stage, as demonstrated above.

4. Summary

We have presented our comprehensive phase-field model for simulating diffusional phase microstructure evolution at solid surfaces. The model integrates the necessary physical contributions such as elastic inhomogeneity and anisotropy, diffusion mobility anisotropy, interfacial energy anisotropy, and possible solute-surface interactions that may determine the surface phase behaviors. Employing the model and the physical parameters of Li_XFePO_4, we performed computer simulations to systematically examine the surface phase behaviors. Our phase-field model predicted two surface spinodal decomposition modes: the *surface mode of coherent spinodal decomposition* and the *surface-directed spinodal decomposition mode*. We confirmed that the contributions of these surface modes become more significant factors in determining the phase microstructure of an entire particle as the particle size decreases. It was also shown that the features of the operating phase separation modes are strongly dependent on the diffusion mobility anisotropy and the interfacial energy anisotropy, leading to a variety of different possible surface phase microstructures. Furthermore, the phase microstructure of a particle interior at the later stage responds to the surface phase domain structure at the early stage when the diffusion mobility is highly anisotropic. Under these conditions, it should be possible to tailor the internal phase microstructure of the solid particle by controlling the surface phase microstructure.

In summary, our results offer a more detailed understanding of operating phase separation mechanisms and their responses under various conditions, which can provide useful guidance for manipulating internal phase microstructures of materials. It should be noted that our integrated phase-field model is generic and can be therefore applied to any phase-separating materials system with surfaces. Consequently, our modeling and simulation framework may be utilized to find strategies for controlling and designing the diffusion-controlled phase microstructures of particles across a broad range of possible applications.

Acknowledgement

This work was performed under the auspices of the U.S. Department of Energy by Lawrence Livermore National Laboratory (LLNL) under Contract DE-AC52-07NA27344. This work was funded by the Laboratory Directed Research and Development Program at LLNL under project tracking code 12-ERD-053. The work at Penn State is also partially supported by NSF under CMMI-1235092. Helpful discussions with M. Tang, Y.M. Wang, J.C. Ye, J. Lee, Y. An, and M. Ong (LLNL) are acknowledged.

Figure captions

Figure 1. Schematic descriptions of (a) the surface structure described by a domain parameter (ψ) and (b) the computational setup for the simulations.

Figure 2. (a) Simulated microstructures at t=50000Δt and (b) the Li-rich phase volume fraction evolution with time for different magnitudes of m^*. The *a*-*b* cross-section view of microstructures at t=50000Δt for the cases where (c) only surface coherency relaxation, (d) only the solute-surface interaction, and (e) both surface coherency relaxation and the solute-surface interaction are considered.

Figure 3. The *a*-*b* cross-section view of simulated phase microstructures with different size dimensions at t=100000Δt for (a) m^*=0.00 and (b) m^*=0.25.

Figure 4. Temporal evolution of phase separation when the diffusion mobility of an entire particle is highly anisotropic ($M_{11}(=M_{33})/M_{22}=0.001$) at (a) the early stage and (c) the later stage, and (b) the cross-section view of the simulated microstructure with the less anisotropic diffusion mobility ($M_{11}(=M_{33})/M_{22}=0.1$).

Figure 5 (a) The simulated microstructure of controlled surface phase domains by the spatially inhomogeneous diffusion mobility and (b) the evolution of Li rich phase volume fraction for different types of diffusion mobility configurations.

Figure 6. (a) The *a*-*b* cross-section view of simulated microstructures for different {010} interfacial energies (κ_{22}^{c}) at t=50000Δt, and (b) the controlled simulation result without the coherency strain energy contribution for the non-dimensionalized $\kappa_{22}^{c,*}$=0.2.

Figure 7. The *a*-*b* cross-section view of temporal phase evolution with both the anisotropic diffusion mobility ($M_{11}(=M_{33})/M_{22}=0.001$) and the anisotropic interfacial energy ($\kappa_{22}^{c,*}$ (=0.2)< $\kappa_{11}^{c,*}=\kappa_{33}^{c,*}$ (=0.5)).

Appendix. Derivation of the dispersion relation $\omega(\vec{k})$

To derive the dispersion relation between the amplification factor ω and the corresponding wave vector $\vec{k}$ against the given compositional fluctuations ($\sim e^{\omega t} \cdot e^{i\vec{k}\cdot\vec{r}}$), we consider the early stage of the decomposition of a homogeneous solid solution with X=X_0. Let us consider the governing equation (*i.e.*, Cahn-Hilliard equation, Eq. (4)) incorporating anisotropic elasticity, diffusion mobility, and interfacial energy. Since only diagonal components are non-zero in our case, the equation can be simplified as follows:

$$\begin{aligned}\frac{\partial X}{\partial t} &= \nabla_i \cdot \left[M_{ii} \nabla_i \left(\frac{\delta F}{\delta X} \right) \right] = \nabla_i \cdot \left[M_{ii} \nabla_i \left\{ \left(\frac{\delta F_{inc}}{\delta X} \right) + \left(\frac{\delta F_{grad}}{\delta X} \right) + \left(\frac{\delta F_{coh}}{\delta X} \right) \right\} \right] \\ &= \nabla_i \cdot \left[M_{ii} \nabla_i \left\{ \left(\frac{\partial f_{inc}}{\partial X} \right) - \kappa^c_{kk} \nabla_k \cdot \nabla_k X + \left(\frac{\delta F_{coh}}{\delta X} \right) \right\} \right] \\ &= \nabla_i \cdot \left[M_{ii} \left\{ \left(\frac{\partial^2 f_{inc}}{\partial X^2} \right) \nabla_i X - \nabla_i (\kappa^c_{kk} \nabla_k \cdot \nabla_k X) + \nabla_i \left(\frac{\delta F_{coh}}{\delta X} \right) \right\} \right],\end{aligned} \tag{A1}$$

where $F_{inc} = \int_V f_{inc} d^3 r$, $F_{grad} = \int_V f_{grad} d^3 r$, and $F_{coh} = \int_V f_{coh} d^3 r$. We linearize Eq. (A1) by assuming that the elastic modulus is homogeneous and $\partial^2 f_{inc} / \partial X^2$ is constant [58]. We note that F_{coh} becomes

$$F_{coh} = \frac{1}{2} \int_{\tilde{V}} \frac{d^3 k}{(2\pi)^3} [B(\vec{n}) \cdot \tilde{X}^2], \tag{A2}$$

when the elastic modulus is homogeneous and anisotropic according to Khachaturyan's microelasticity theory [55], where $B(\vec{n}) = C_{ijkl} \varepsilon^m_{ij} \varepsilon^m_{kl} - n_i \sigma^0_{ij} \Omega_{jl}(\vec{n}) \sigma^0_{lm} n_m$, $\vec{n} = \vec{k} / |\vec{k}|$, ε^m_{ij} is the misfit strain tensor between the two end phases ($FePO_4$ and $LiFePO_4$ in our case), $\sigma^0_{ij} = C_{ijkl} \varepsilon^m_{kl}$, $\Omega^{-1}_{ij}(\vec{n}) = C_{iklj} n_k n_l$, and tilde (~) represents the Fourier transform. For the homogeneous elastic modulus (C_{ijkl}), we use the average elastic modulus (*i.e.*, $C_{ijkl} = C^{FP}_{ijkl} \cdot (1 - X_0) + C^{LFP}_{ijkl} \cdot X_0$). The variational derivative of F_{coh} with respect to X then becomes

$$\frac{\delta F_{coh}}{\delta X} = \int_{\tilde{V}} \frac{d^3 k}{(2\pi)^3} [B(\vec{n}) \cdot \tilde{X}] \cdot e^{i\vec{k}\cdot\vec{r}}, \tag{A3}$$

Eq. (A3) shows that $\delta F_{coh}/\delta X$ is the inverse Fourier transform of $[B(\vec{n}) \cdot X]$. Taking the Fourier transform of Eq. (A1) and using Eq. (A3), we obtain the following:

$$\begin{aligned}\frac{\partial \tilde{X}}{\partial t} &= ik_i\left[M_{ii}\left\{\left(\frac{\partial^2 f_{inc}}{\partial X^2}\right)ik_i\tilde{X} - ik_i(-\kappa^c_{kk}k_k^2\tilde{X}) + ik_i\left(\frac{\delta F_{coh}}{\delta X}\right)_k\right\}\right] \\ &= ik_i\left[M_{ii}\left\{\left(\frac{\partial^2 f_{inc}}{\partial X^2}\right)ik_i\tilde{X} - ik_i(-\kappa^c_{kk}k_k^2\tilde{X}) + ik_iB(\vec{n})\tilde{X}\right\}\right] \\ &= -(M_{ii}k_i^2)\cdot\left[f''_{inc} + \kappa^c_{kk}k_k^2 + B(\vec{n})\right]\tilde{X}.\end{aligned} \tag{A4}$$

The solution of the above differential equation in a reciprocal space is determined as

$$\begin{aligned}\tilde{X}(\vec{k},t) &= \tilde{X}(\vec{k},t=0)\cdot\exp(-[M_{ii}k_i^2]\cdot[f''_{inc} + \kappa^c_{kk}k_k^2 + B(\vec{n})]\cdot t) \\ &= \tilde{X}(\vec{k},t=0)\cdot\exp(\omega(\vec{k})\cdot t).\end{aligned} \tag{A5}$$

We note that $\tilde{X}(\vec{k},t)$ represents the amplitude associated with each Fourier mode $\vec{k}$ of compositional fluctuation (*i.e.*, the Fourier transform of X) expressed in a Fourier representation:

$$X(\vec{r},t) = \int_{\tilde{V}}\frac{d^3k}{(2\pi)^3}\tilde{X}(\vec{k},t)\cdot e^{i\vec{k}\cdot\vec{r}}. \tag{A6}$$

Therefore, the general dispersion relation between the amplification factor ω and the corresponding wave vector $\vec{k}$ is determined as follows:

$$\omega(\vec{k}) = -[M_{11}k_1^2 + M_{22}k_2^2 + M_{33}k_3^2]\cdot[f''_{inc}(X_0) + \kappa^c_{11}k_1^2 + \kappa^c_{22}k_2^2 + \kappa^c_{33}k_3^2 + B(\vec{n})]. \tag{A7}$$

We emphasize here that $B(\vec{n}) \neq 0$ inside the bulk, and the dispersion relation inside the bulk is anisotropic due to the orientation-dependent $B(\vec{n})$. On the other hand, at surfaces, $B(\vec{n}) = 0$ due to the zero surface traction boundary condition. Therefore, the dispersion relation against the surface compositional fluctuations reduces to

$$\omega^{surf}(\vec{k}) = -[M_{11}k_1^2 + M_{22}k_2^2 + M_{33}k_3^2]\cdot[f''_{inc}(X_0) + \kappa^c_{11}k_1^2 + \kappa^c_{22}k_2^2 + \kappa^c_{33}k_3^2]. \tag{A8}$$

The dispersion relation can provide the maximally growing wavelength $\lambda_{\max}$ (or wave vector $\vec{k}_{\max}$) that maximizes ω, which determines the characteristic length scale of surface/bulk phase domain structure. For example, when both diffusion mobility and interfacial energy are isotropic, the dispersion relation predicts that the maximally growing wavelength $\lambda_{\max}$ ($=2\pi/|\vec{k}_{\max}|$) is 18.8 *n*m ($|\vec{k}_{\max}|$=0.33 *n*m^{-1}, aligned along $\vec{n}$=(0.89,0.00,0.45)) inside the bulk and 11.1 *n*m at surfaces ($|\vec{k}_{\max}|$=0.57 *n*m^{-1}, aligned along the *a*-*c* plane (or normal to $\vec{k} = (0,k_2,0)$)). We tabulate the computed maximally growing wavelengths and corresponding non-dimensionalized amplification factors ($\omega^{*}_{\max} = \omega^{*}(\vec{k}_{\max})$) in Table A1 using Eqs. (A7) and (A8) for the representative cases simulated in this article.

Table A1. Maximally growing wavelengths and corresponding amplification factors

Cases	**Bulk**		**Surface**	
	$\lambda^{bulk}_{\max}$	$\omega^{bulk,*}_{\max}$	$\lambda^{surface}_{\max}$	$\omega^{surface,*}_{\max}$
Isotropic M_{ij} **Isotropic** κ^{c}_{ij}	18.8 *n*m	6.04×10^{-3}	11.1 *n*m ($\perp \vec{k}_2$)	5.17×10^{-2} ($\perp \vec{k}_2$)
Anisotropic M_{ij} **Isotropic** κ^{c}_{ij}	21.5 *n*m	0.92×10^{-3}	11.2 *n*m ($\parallel \vec{k}_2$)	5.17×10^{-2} ($\parallel \vec{k}_2$)
Isotropic M_{ij} **Anisotropic** κ^{c}_{ij}	18.8 *n*m	6.04×10^{-3}	7.0 *n*m ($\parallel \vec{k}_2$)	12.93×10^{-2} ($\parallel \vec{k}_2$)
Anisotropic M_{ij} **Anisotropic** κ^{c}_{ij}	20.1 *n*m	1.18×10^{-3}	7.0 *n*m ($\parallel \vec{k}_2$)	12.93×10^{-2} ($\parallel \vec{k}_2$)

Note I) Anisotropic M_{ij}: $M_{11} = M_{33} = 0.001M_{22}$, Anisotropic κ^{c}_{ij}: $\kappa^{c,*}_{11} = \kappa^{c,*}_{33} = 0.5, \kappa^{c,*}_{22} = 0.2$

Note II) ($\perp \vec{k}_2$): The maximally growing wave is aligned normal to $\vec{k}_2 = (0, k_2, 0)$, ($\parallel \vec{k}_2$): The maximally growing wave is aligned along with $\vec{k}_2 = (0, k_2, 0)$

References

[1] Tang M, Carter WC, Chiang YM. Electrochemically Driven Phase Transitions in Insertion Electrodes or Lithium-Ion Batteries: Examples in Lithium Metal Phosphate Olivines. In: Clarke DR, Ruhle M, Zok F, editors. Annual Review of Materials Research, Vol 40. Palo Alto: Annual Reviews; 2010. p. 501.
[2] Padhi AK, Nanjundaswamy KS, Goodenough JB. J Electrochem Soc 1997;144:1188.
[3] Delacourt C, Poizot P, Tarascon JM, Masquelier C. Nat Mater 2005;4:254.
[4] Yamada A, Koizumi H, Nishimura SI, Sonoyama N, Kanno R, Yonemura M, et al. Nat Mater 2006;5:357.
[5] Meethong N, Huang HYS, Carter WC, Chiang YM. Electrochem Solid State Lett 2007;10:A134.
[6] Meethong N, Huang HYS, Speakman SA, Carter WC, Chiang YM. Adv Funct Mater 2007;17:1115.
[7] Gibot P, Casas-Cabanas M, Laffont L, Levasseur S, Carlach P, Hamelet S, et al. Nat Mater 2008;7:741.
[8] Van der Ven A, Garikipati K, Kim S, Wagemaker M. J Electrochem Soc 2009;156:A949.
[9] Wagemaker M, Mulder FM, Van der Ven A. Adv Mater 2009;21:2703.
[10] Malik R, Zhou F, Ceder G. Nat Mater 2011;10:587.
[11] Ichitsubo T, Doi T, Tokuda K, Matsubara E, Kida T, Kawaguchi T, et al. J Mater Chem A 2013;1:14532.
[12] Chen LQ. Ann Rev Mater Res 2002;32:113.
[13] Boettinger WJ, Warren JA, Beckermann C, Karma A. Ann Rev Mater Res 2002;32:163.
[14] Emmerich H. Adv Phys 2008;57:1.
[15] Moelans N, Blanpain B, Wollants P. Calphad-Comput Coupling Ph Diagrams Thermochem 2008;32:268.
[16] Steinbach I. Model Simul Mater Sci Eng 2009;17:31.
[17] Han BC, Van der Ven A, Morgan D, Ceder G. Electrochim Acta 2004;49:4691.
[18] Singh GK, Ceder G, Bazant MZ. Electrochim Acta 2008;53:7599.
[19] Burch D, Bazant MZ. Nano Lett 2009;9:3795.
[20] Bai P, Cogswell DA, Bazant MZ. Nano Lett 2011;11:4890.
[21] Cogswell DA, Bazant MZ. ACS Nano 2012;6:2215.
[22] Cogswell DA, Bazant MZ. Nano Lett 2013;13:3036.
[23] Bazant MZ. Accounts Chem Res 2013;46:1144.
[24] Tang M, Huang HY, Meethong N, Kao YH, Carter WC, Chiang YM. Chem Mat 2009;21:1557.
[25] Tang M, Carter WC, Belak JF, Chiang YM. Electrochim Acta 2010;56:969.
[26] Tang M, Belak JF, Dorr MR. J Phys Chem C 2011;115:4922.
[27] Ichitsubo T, Tokuda K, Yagi S, Kawamori M, Kawaguchi T, Doi T, et al. J Mater Chem A 2013;1:2567.
[28] Cahn JW, Hilliard JE. J Chem Phys 1958;28:258.
[29] Cahn JW. Acta Metallurgica 1962;10:789.
[30] Gronhagen K, Agren J. Acta Mater 2007;55:955.
[31] Heo TW, Bhattacharyya S, Chen LQ. Acta Mater 2011;59:7800.
[32] Wynblatt P, Chatain D. Metall Mater Trans A-Phys Metall Mater Sci 2006;37A:2595.
[33] Wang L, Zhou F, Meng YS, Ceder G. Phys Rev B 2007;76:11.
[34] Yu HC, Chen HY, Thornton K. Model Simul Mater Sci Eng 2012;20:41.
[35] Bhattacharyya S, Heo TW, Chang K, Chen LQ. Model Simul Mater Sci Eng 2011;19:17.
[36] Bhattacharyya S, Heo TW, Chang K, Chen LQ. Commun Comput Phys 2012;11:726.
[37] Heo TW, Bhattacharyya S, Chen LQ. Philos Mag 2013;93:1468.
[38] Hu SY, Chen LQ. Acta Mater 2001;49:1879.
[39] Yu P, Hu SY, Chen LQ, Du Q. J Comput Phys 2005;208:34.

[40] Cahn JW. Acta Metallurgica 1961;9:795.
[41] Zhu JZ, Chen LQ, Shen J, Tikare V. Phys Rev E 1999;60:3564.
[42] Chen LQ, Shen J. Comput Phys Commun 1998;108:147.
[43] Maxisch T, Ceder G. Phys Rev B 2006;73:4.
[44] Chen GY, Song XY, Richardson TJ. Electrochem Solid State Lett 2006;9:A295.
[45] Tang M, Karma A. Phys Rev Lett 2012;108:5.
[46] Jones RAL, Norton LJ, Kramer EJ, Bates FS, Wiltzius P. Phys Rev Lett 1991;66:1326.
[47] Puri S, Binder K. Phys Rev E 1994;49:5359.
[48] Frisch HL, Nielaba P, Binder K. Phys Rev E 1995;52:2848.
[49] Puri S, Binder K, Frisch HL. Phys Rev E 1997;56:6991.
[50] Binder K, Puri S, Frisch HL. Faraday Discuss 1999;112:103.
[51] Wise SM, Kim JS, Johnson WC. Thin Solid Films 2005;473:151.
[52] Nye JF. Physical Properties of Crystals. New York: Oxford University Press; 1985.
[53] Morgan D, Van der Ven A, Ceder G. Electrochem Solid State Lett 2004;7:A30.
[54] Islam MS, Driscoll DJ, Fisher CAJ, Slater PR. Chem Mat 2005;17:5085.
[55] Khachaturyan AG. Theory of Structural Transformations in Solids. New York: John Wiley & Sons; 1983.
[56] Cahn JW. J Chem Phys 1965;42:93.
[57] Abdellahi A, Akyildiz O, Malik R, Thornton K, Ceder G. J Mater Chem A 2014;2:15437.
[58] Balluffi RW, Allen S, Carter WC. Kinetics of Materials: Wiley; 2005.

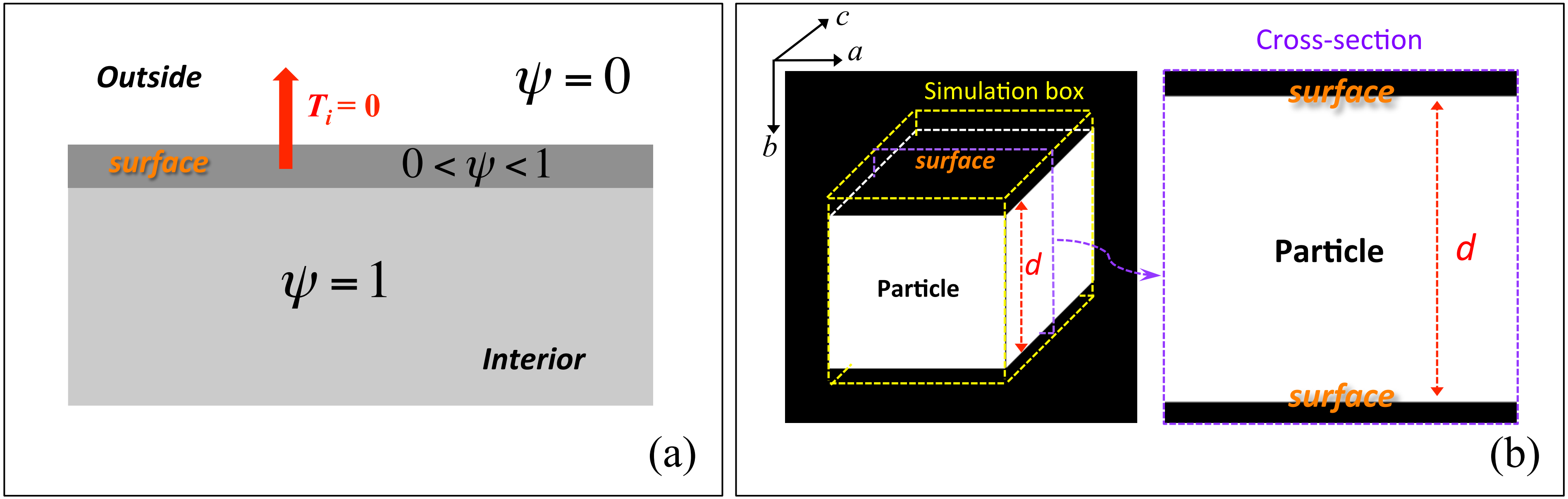
Outside
$T_i = 0$
$\psi = 0$
surface
$0 < \psi < 1$
$\psi = 1$
Interior
(a)
c
a
b
Simulation box
surface
Particle
d
Cross-section
surface
Particle
d
surface
(b)

Fig. 1

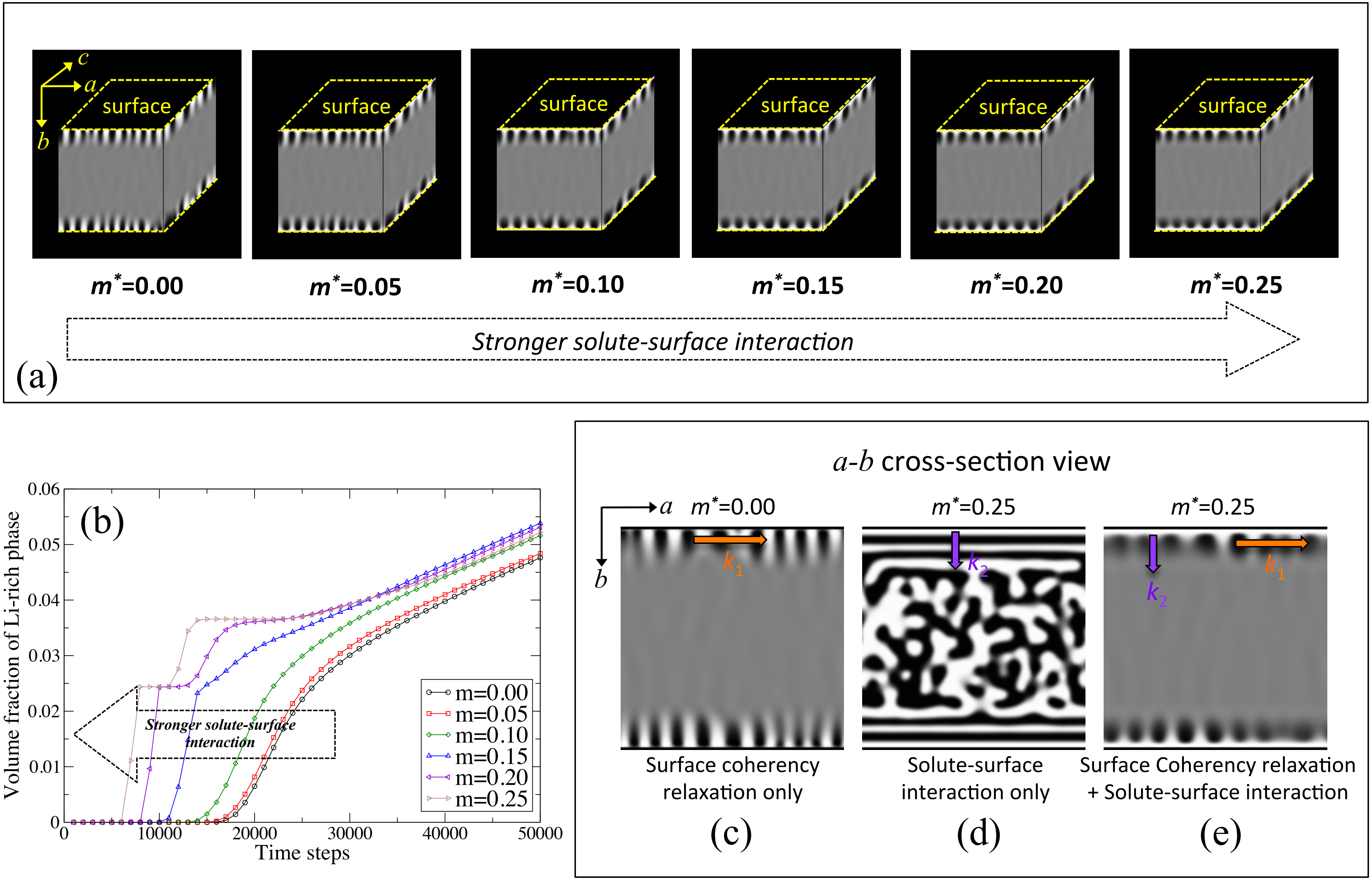
c
a
b
surface
m*=0.00
m*=0.05
m*=0.10
m*=0.15
m*=0.20
m*=0.25
Stronger solute-surface interaction
(a)
(b)
Volume fraction of Li-rich phase
0.06
0.05
0.04
0.03
0.02
0.01
0
Time steps
0
10000
20000
30000
40000
50000
Stronger solute-surface interaction
m=0.00
m=0.05
m=0.10
m=0.15
m=0.20
m=0.25
a-b cross-section view
a
b
m*=0.00
m*=0.25
m*=0.25
k1
k2
k2
k1
Surface coherency relaxation only
Solute-surface interaction only
Surface Coherency relaxation + Solute-surface interaction
(c)
(d)
(e)

Fig. 2

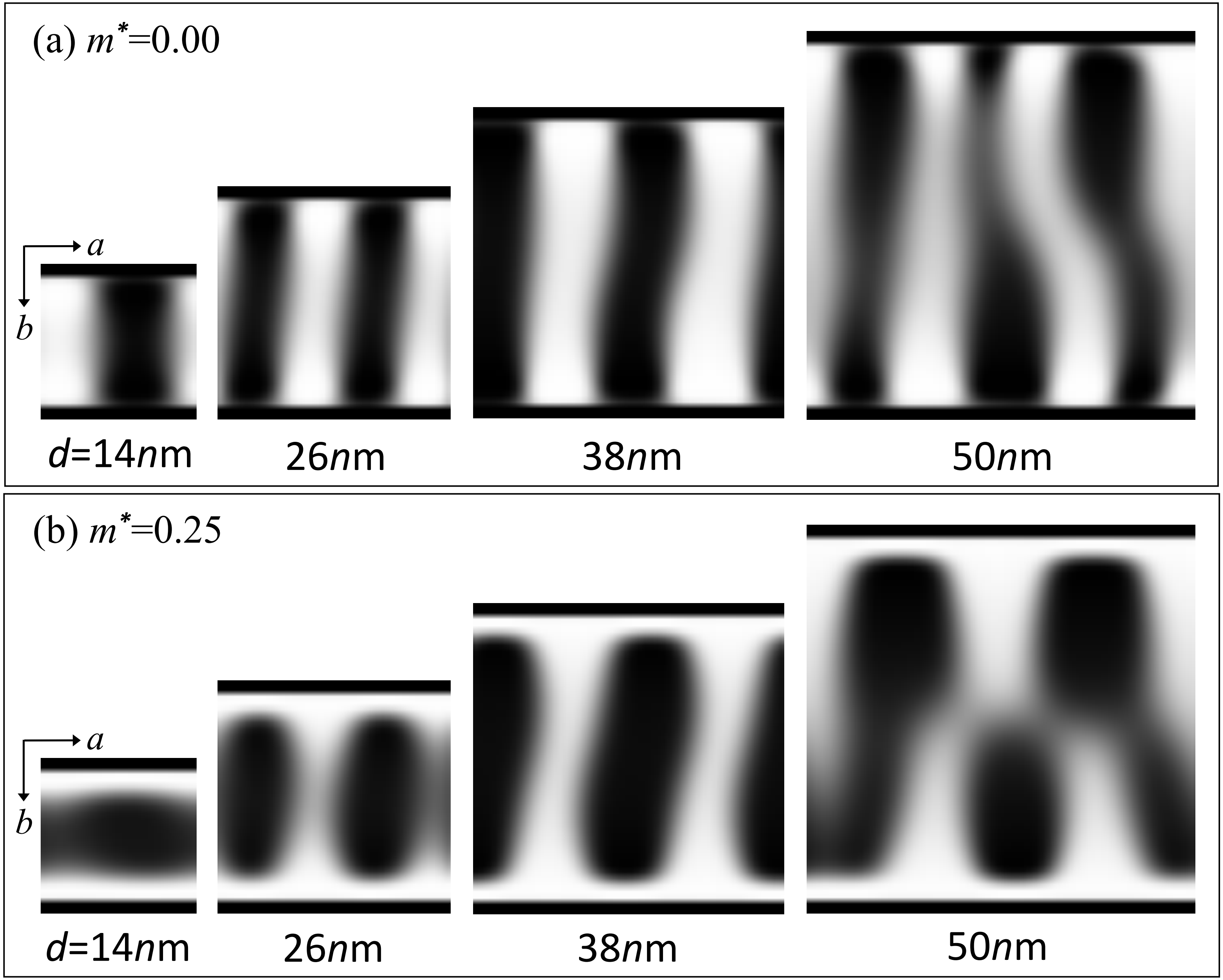
(a) m^*=0.00
a
b
d=14nm
26nm
38nm
50nm
(b) m^*=0.25
a
b
d=14nm
26nm
38nm
50nm

Fig. 3

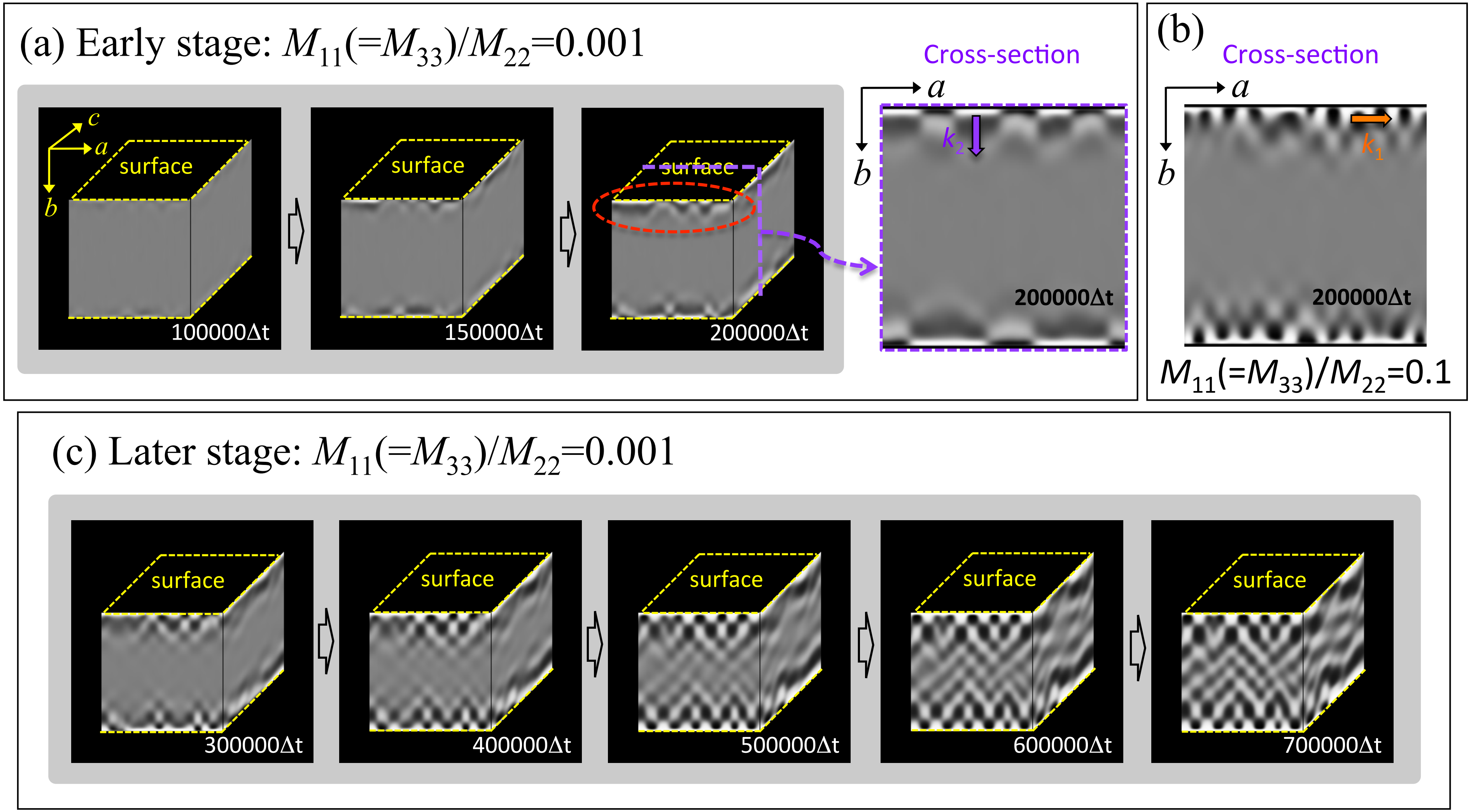
(a) Early stage: $M_{11}(=M_{33})/M_{22}=0.001$
c
a
b
surface
100000Δt
150000Δt
200000Δt
Cross-section
a
b
k_2
200000Δt
(b)
Cross-section
a
b
k_1
200000Δt
$M_{11}(=M_{33})/M_{22}=0.1$
(c) Later stage: $M_{11}(=M_{33})/M_{22}=0.001$
surface
300000Δt
400000Δt
500000Δt
600000Δt
700000Δt

Fig. 4

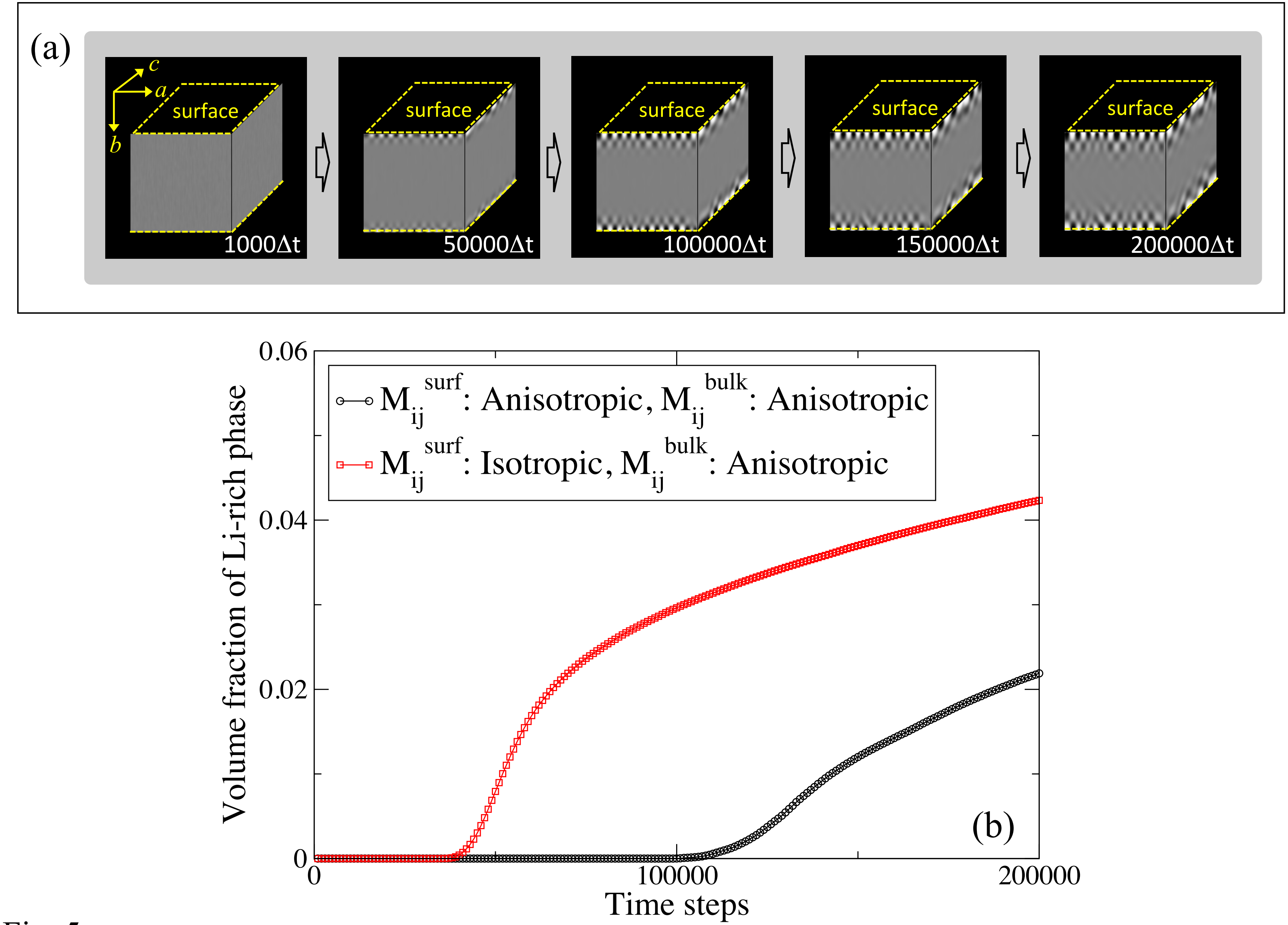
(a)
c
a
b
surface
1000Δt
50000Δt
100000Δt
150000Δt
200000Δt
M_{ij}^{surf}: Anisotropic, M_{ij}^{bulk}: Anisotropic
M_{ij}^{surf}: Isotropic, M_{ij}^{bulk}: Anisotropic
Volume fraction of Li-rich phase
0
0.02
0.04
0.06
0
100000
200000
Time steps
(b)

Fig. 5

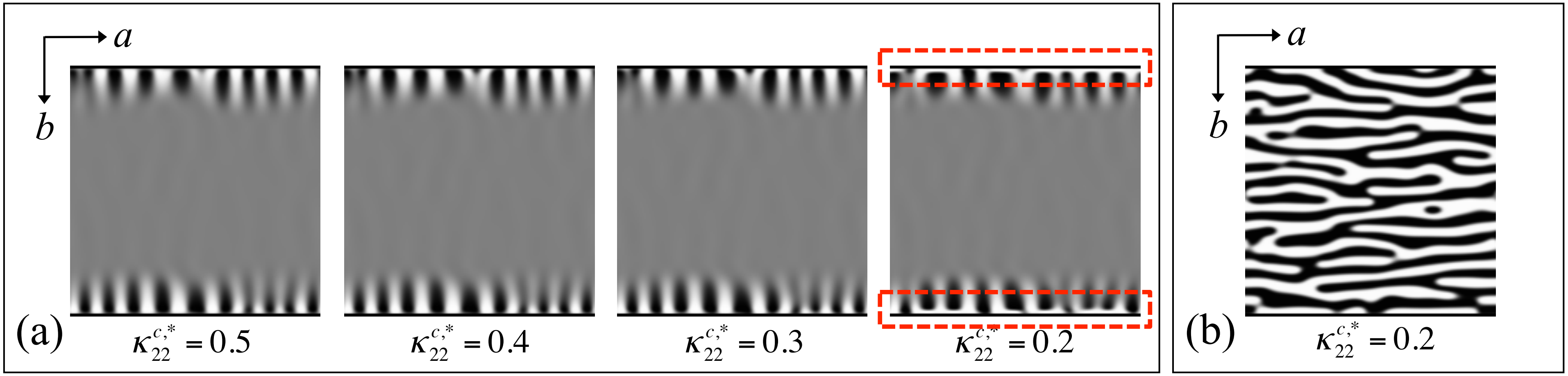
a
b
(a)
$\kappa_{22}^{c,*}=0.5$
$\kappa_{22}^{c,*}=0.4$
$\kappa_{22}^{c,*}=0.3$
$\kappa_{22}^{c,*}=0.2$
a
b
(b)
$\kappa_{22}^{c,*}=0.2$

Fig. 6

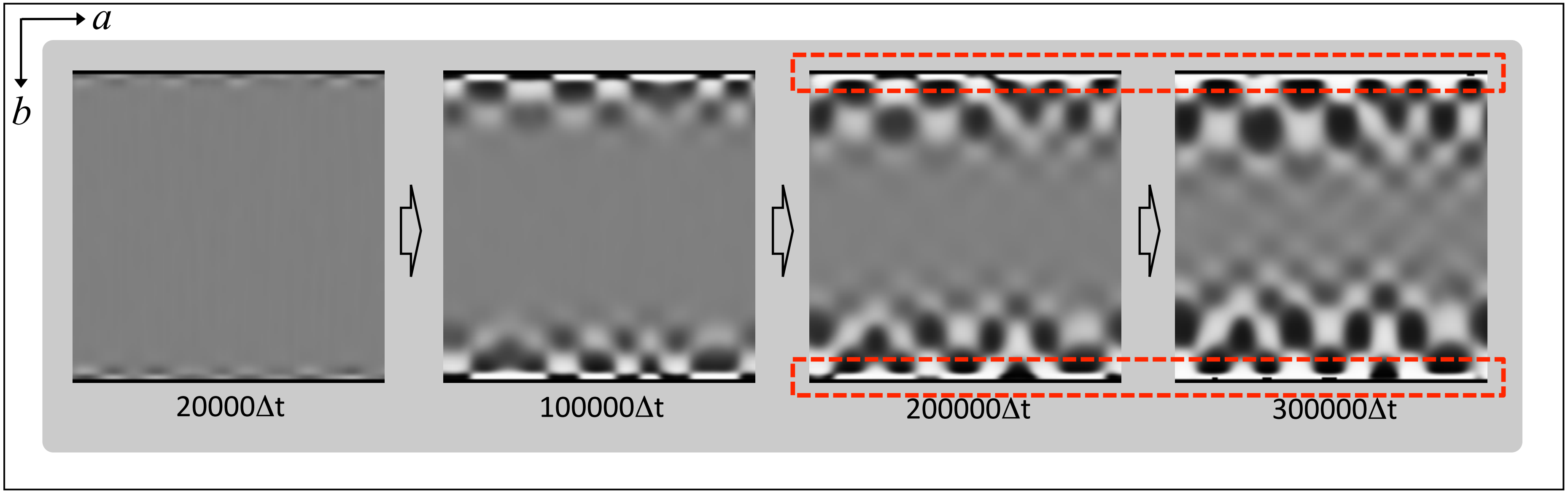

Fig. 7

Graphical abstract

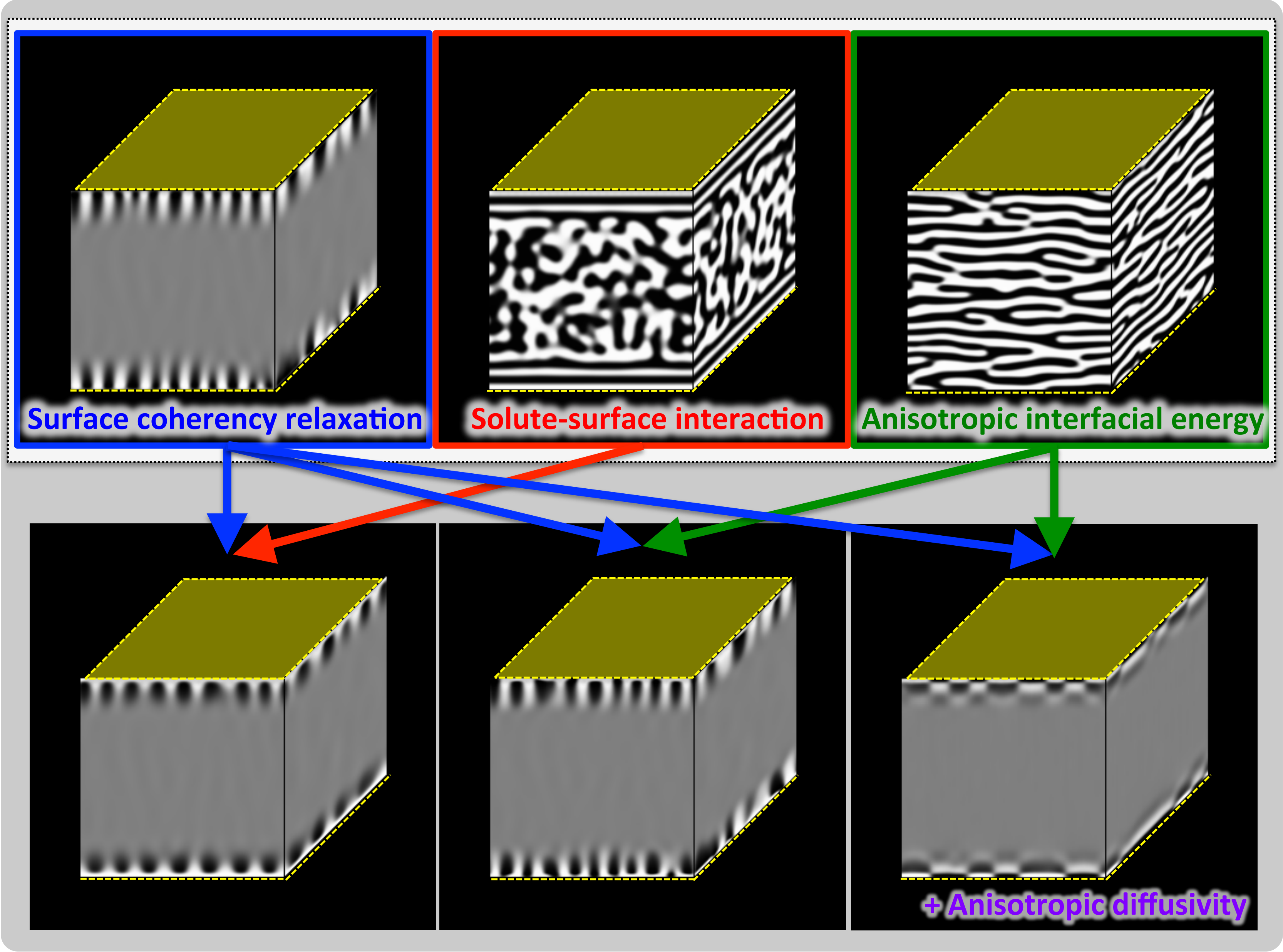
Surface coherency relaxation
Solute-surface interaction
Anisotropic interfacial energy
+ Anisotropic diffusivity